Monthly Notices of the ROYAL ASTRONOMICAL SOCIETY

Mon. Not. R. Astron. Soc. **413,** 149–161 (2011) doi:10.1111/j.1365-2966.2010.18116.x

Gas streaming motions towards the nucleus of M81

Allan Schnorr Müller,[1★] Thaisa Storchi-Bergmann,[1] Rogemar A. Riffel,[2] Fabricio Ferrari,[3] J. E. Steiner,[4] David J. Axon[5,6] and Andrew Robinson[5]

[1]*Instituto de Física, Universidade Federal do Rio Grande do Sul, 91501-970 Porto Alegre, RS, Brazil*
[2]*Universidade Federal de Santa Maria, Departamento de Física, 97105-900 Santa Maria, RS, Brazil*
[3]*Universidade Federal do Pampa, Campus Bagé, 96412-420 Bagé, RS, Brazil*
[4]*Instituto de Astronomia, Geofísica e Ciências Atmosféricas, Universidade de São Paulo, 05508-900 São Paulo, SP, Brazil*
[5]*Physics Department, Rochester Institute of Technology, Rochester, NY 14623, USA*
[6]*University of Sussex, School of Mathematical and Physical Sciences, University of Sussex, Sussex House, Brighton BN1 9RH*

Accepted 2010 November 26. Received 2010 November 12; in original form 2010 June 7

ABSTRACT

We present two-dimensional stellar and gaseous kinematics of the inner $120 \times 250\,\mathrm{pc}^2$ of the LINER/Seyfert 1 galaxy M81, from optical spectra obtained with the Gemini Multi-Object Spectrograph (GMOS) integral field spectrograph on the Gemini-North telescope at a spatial resolution of $\approx$10 pc. The stellar velocity field shows circular rotation and, overall, is very similar to the published large-scale velocity field, but deviations are observed close to the minor axis which can be attributed to stellar motions possibly associated with a nuclear bar. The stellar velocity dispersion of the bulge is $162 \pm 15\,\mathrm{km\,s^{-1}}$, in good agreement with previous measurements and leading to a black hole mass of $M_{\mathrm{BH}} = 5.5^{+3.6}_{-2.0} \times 10^7\,\mathrm{M}_\odot$ based on the M_{BH}–σ relationship. The gas kinematics is dominated by non-circular motions and the subtraction of the stellar velocity field reveals blueshifts of $\approx -100\,\mathrm{km\,s^{-1}}$ on the far side of the galaxy and a few redshifts on the near side. These characteristics can be interpreted in terms of streaming towards the centre if the gas is in the plane. On the basis of the observed velocities and geometry of the flow, we estimate a mass inflow rate in ionized gas of $\approx 4.0 \times 10^{-3}\,\mathrm{M}_\odot\,\mathrm{yr}^{-1}$, which is of the order of the accretion rate necessary to power the LINER nucleus of M81. We have also applied the technique of principal component analysis (PCA) to our data, which reveals the presence of a rotating nuclear gas disc within $\approx$50 pc from the nucleus and a compact outflow, approximately perpendicular to the disc. The PCA combined with the observed gas velocity field shows that the nuclear disc is being fed by gas circulating in the galaxy plane. The presence of the outflow is supported by a compact jet seen in radio observations at a similar orientation, as well as by an enhancement of the [O I]/Hα line ratio, probably resulting from shock excitation of the circumnuclear gas by the radio jet. With these observations we are thus resolving both the feeding – via the nuclear disc and observed gas inflow, and the feedback – via the outflow, around the low-luminosity active nucleus of M81.

Key words: galaxies: active – galaxies: individual: M81 – galaxies: jets – galaxies: kinematics and dynamics – galaxies: nuclei – galaxies: Seyfert.

1 INTRODUCTION

It is widely accepted that the radiation emitted by an active galactic nucleus (AGN) is a result of accretion on to the central supermassive black hole (SMBH). However, the exact nature of the mechanisms responsible for transferring mass from galactic scales down to nuclear scales to feed the SMBH is still an open question. Theoretical studies and simulations (Shlosman, Begelman & Frank 1990; Emsellem, Goudfrooij & Ferruit 2003; Knapen 2005; Emsellem et al. 2006) have shown that non-axisymmetric potentials efficiently promote gas inflow towards the inner regions (Englmaier & Shlosman 2004). Imaging studies have revealed that structures such as small-scale discs or nuclear bars and associated spiral arms are frequently observed in the inner kiloparsec of active galaxies (Erwin & Sparke 1999; Pogge & Martini 2002; Laine et al. 2003), although

★E-mail: allanschnorr@gmail.com

© 2011 The Authors
Monthly Notices of the Royal Astronomical Society © 2011 RAS

Downloaded from http://mnras.oxfordjournals.org/ at FundaÃ§Ã£o CoordenaÃ§Ã£o de AperfeiÃ§oamento de Pessoal de NÃ-vel Superior on February 25, 2014

Shaw et al. (1993) raise important points about the identification of nuclear bars.

While bars can be effective in transporting gas into the inner few hundred parsecs, the fundamental problem of how gas gets from there down to the SMBH has remained unsolved. Recently, Simões Lopes et al. (2007) have shown a strong correlation between the presence of nuclear dust structures (filaments, spirals and discs) and activity in galaxies. García-Burillo et al. (2005) have argued that stellar gravity torques are also a mechanism that can drive gas inwards at least to a few hundred parsecs of the nuclei.

Inward gas streaming on galactic scales has only been observed in a few objects. Adler & Westpfahl (1996) found gas inflows along the spirals arms of M81 and Mundell & Shone (1999) found inflows along the bar of NGC 4151. An important recent development has been the recognition of streaming motions on nuclear scales in both the ionized and molecular gas. In the ionized gas, inflows have been observed in the central region of NGC 1097 (Fathi et al. 2006) and NGC 6951 (Storchi-Bergmann et al. 2007) and in molecular hydrogen (H_2) in NGC 1068 (Sánchez et al. 2009), NGC 4051 (Riffel et al. 2008), NGC 1097 (Davies et al. 2009) and Mrk 1066 (Riffel & Storchi-Bergmann 2010).

With the goal of looking for more cases of inward streaming motions we began a project to map the gaseous kinematics around nearby AGN. In the present work, we present results obtained from integral field spectroscopic observations of the nuclear region of M81, a spiral galaxy with Hubble type SA(s)ab. At a distance of 3.5 Mpc (Paturel et al. 2002), corresponding to a scale of 17 pc arcsec^{-1}, M81 harbours the nearest directly observable low-luminosity AGN, classified as low-ionization nuclear emission-line region (LINER) / Seyfert 1 (Heckman 1980; Peimbert & Torres-Peimbert 1981). Because of M81 proximity, the AGN has been the subject of many studies. It was found to vary with time at optical (Bower et al. 1996), radio (Ho 1999) and X-ray wavelengths (Iyomoto & Makishima 2001). The nuclear spectrum presents broad optical and UV emission lines (Peimbert & Torres-Peimbert 1981) and a featureless UV continuum (Ho, Filippenko & Sargent 1996). Devereux, Ford & Jacoby (1997) detected a compact optical/UV continuum source, and Bietenholz, Bartel & Rupen (2000) detected an ultra-compact radio source associated with a radio jet. Its accretion physics was studied by Markoff et al. (2008).

The present paper is organized as follows. In Section 2 we describe the observations and reductions. In Section 3 we present the results. In Section 4 we present the stellar and gaseous kinematics. In Section 5 we present the gas flux distributions and ratios, and in Section 6 we discuss our results and an alternative method for the analysis of the gas kinematics using the technique of principal component analysis (PCA). In Section 6.3 we present an estimate of the mass inflow rate, and in Section 7 we present our conclusions.

2 OBSERVATIONS AND REDUCTIONS

The observations were obtained with the Integral Field Unit of the Gemini Multi-Object Spectrograph (GMOS-IFU) at the Gemini-North telescope on the night of 2006 December 31 (Gemini project GN-2006B-Q-94). The observations consisted of three adjacent IFU fields (covering 7×5 arcsec^2 each) resulting in a total angular coverage of 7×15 arcsec^2 around the nucleus, with the longest extent of the field chosen to be along the galaxy major axis as reported by Goad (1976) (position angle PA = 150°). Three exposures of 191 s were obtained for each field, slightly shifted in order to correct for detector defects after combination of the frames. The seeing during the observation was 0.6 arcsec, as measured from the full width at half-maximum (FWHM) of a spatial profile of the galaxy extracted along the broad Hα profile under the assumption that the broad-line region is unresolved. This corresponds to a spatial resolution at the galaxy of 10.2 pc.

The selected wavelength range was 5600–7000 Å, in order to cover the Hα+[N II] $\lambda\lambda$6548,6583 and [S II] $\lambda\lambda$6716,6731 emission lines, observed with the grating GMOS R400-G5305 (set to central wavelength λ 6300 Å) at a spectral resolution of $R \approx 2000$.

The data reduction was performed using specific tasks developed for GMOS data in the GEMINI.GMOS package as well as generic tasks in IRAF.[1] The reduction process comprised bias subtraction, flat-fielding, trimming, wavelength calibration, sky subtraction, relative flux calibration, building of the data cubes at a sampling of 0.1×0.1 arcsec, and finally the alignment and combination of the nine data cubes. Unfortunately, in many of the spectra the position of the [S II] $\lambda\lambda$6716,6731 emission lines on the detector coincided with the position of one of the gaps between the CCDs, thus these lines could not be measured at several locations, as is the case of the spectrum extracted from the position marked as A in Fig. 1. As our data cubes are somewhat oversampled (relative to the seeing), a Gaussian filter with FWHM = 3 pixels was applied to the centroid velocity, velocity dispersion, flux and line ratio maps in order to reduce the noise in the figures.

3 RESULTS

In Fig. 1, we show in the upper-left panel a large-scale image of M81 in the *R* band (Cheng et al. 1997). In the upper-right panel we show an image of the inner 22×22 arcsec^2 of the galaxy obtained with the Wide Field Planetary Camera 2 (WFPC2) through the filter F547M aboard the *Hubble Space Telescope* (*HST*). In the middle-left panel we present a structure map of the WFPC2 *HST* image of M81 (see Simões Lopes et al. 2007), where a large nuclear spiral structure, as delineated by the contrast provided by the dust lanes, can be seen. The rectangle shows the field of view (FOV) covered by the IFU observations. In the middle-right panel we present an image from our IFU observations obtained by integrating the flux within a spectral window containing only continuum. In the lower panel we present three spectra of the galaxy corresponding to locations marked as A, B and N in the IFU image and extracted within apertures of 0.1×0.1 arcsec^2.

The spectrum corresponding to the nucleus (marked as N in Fig. 1) is similar to that obtained previously with the *HST* (Bower et al. 1996; Devereux et al. 2003), showing [O I] $\lambda\lambda$ 6300,6363, [N II] $\lambda\lambda$6548,6583 and [S II] $\lambda\lambda$6717,6731 emission lines, which are broader than in the extranuclear spectra. The broad double peaked Hα profile reported by Bower et al. (1996) is not easily seen in our observations, suggesting that its flux has decreased since 1995, when that spectrum was obtained. Spectra from locations A and B show fainter emission in [N II], Hα and [S II] on top of a strong stellar continuum.

4 KINEMATICS

4.1 Stellar kinematics

The spectra of M81 have a high signal-to-noise ratio in the continuum (see Fig. 1) which has allowed us to use the stellar absorption

[1] IRAF is distributed by the National Optical Astronomy Observatories, which are operated by the Association of Universities for Research in Astronomy, Inc., under cooperative agreement with the National Science Foundation.

Downloaded from http://mnras.oxfordjournals.org/ at FundaÃ§Ã£o CoordenaÃ§Ã£o de AperfeiÃ§oamento de Pessoal de NÃ-vel Superior on February 25, 2014

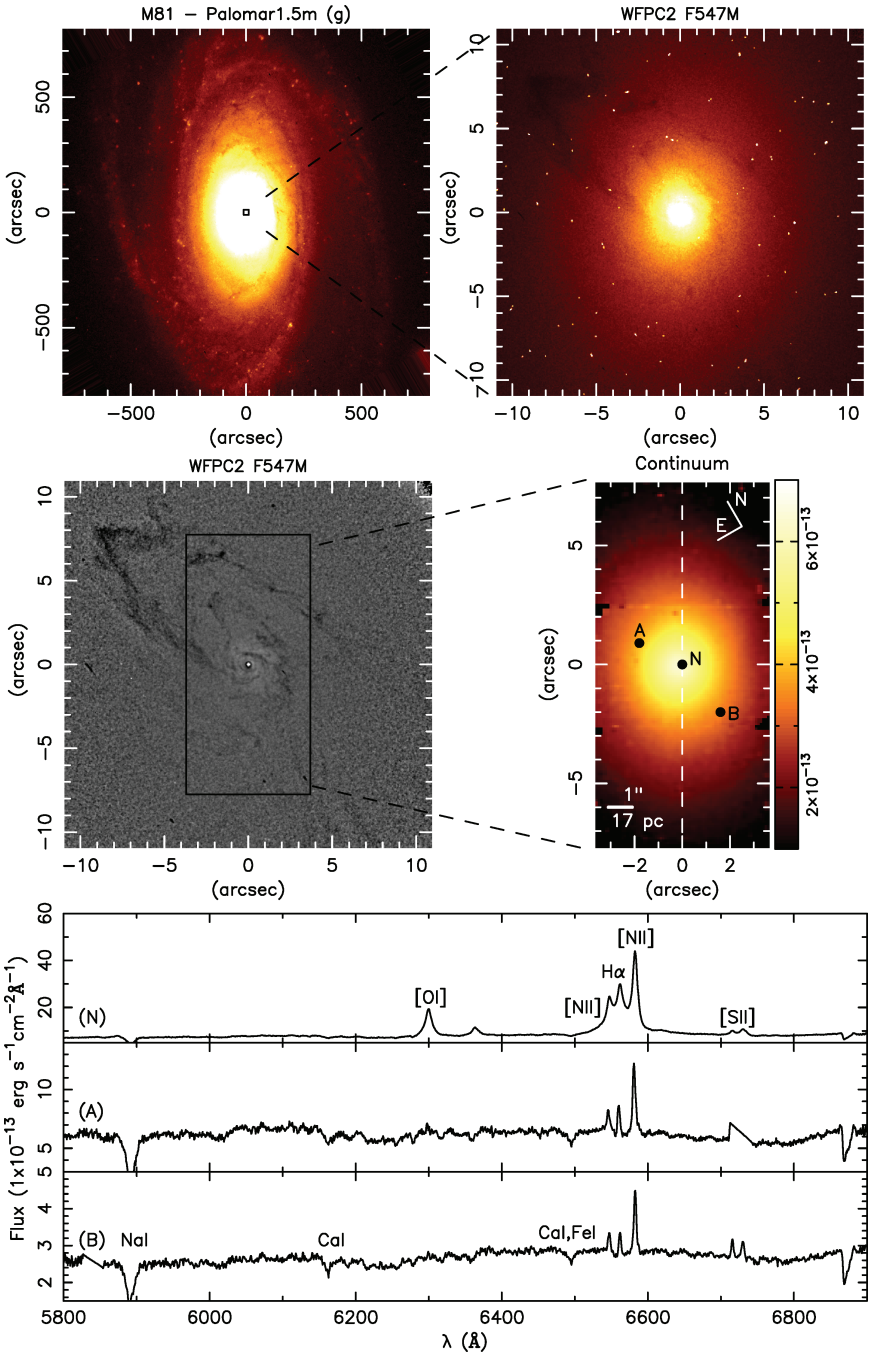

Figure 1. Top left: large-scale image of M81. Top right: WFPC2 image. Middle left: structure map. The rectangle shows the field of the IFU observation. Middle right: continuum image from the IFU spectra (flux in erg cm^2 s^{-1} per pixel). The dashed white line indicates the position of the line of nodes. Bottom: spectra corresponding to the regions marked as N, A and B in the IFU image.

features between 5600 and 7000 Å to derive the stellar kinematics. The penalized pixel fitting technique (pPXF) (Cappellari & Emsellem 2004) was employed to obtain the stellar centroid velocity, velocity dispersion and the Gauss–Hermite moments h_3 and h_4 from each spectrum, using as templates the Bruzual & Charlot (2003) models. Although these models have an instrumental width (σ) of 61 km s^{-1} at 6300 Å, very similar to the value of 66 km s^{-1} of our observations, we have corrected our measurements by this small effect, which results in a decrease of $\approx$1.5 km s^{-1} in the stellar velocity dispersions. Monte Carlo simulations based on the best-fitting absorption spectra were carried out to estimate the errors in the kinematic parameters.

The stellar centroid velocity (V_*) field (top-left panel of Fig. 2) displays a rotation pattern in which the SE side of the galaxy is approaching and the NW side is receding. Under the assumption that the spiral arms are trailing, it can be concluded that the near side of the galaxy is the SW, and the far side is the NE. The calculated errors in the velocity measurement are $\approx$10 km s^{-1} over the whole FOV.

© 2011 The Authors, MNRAS **413,** 149–161
Monthly Notices of the Royal Astronomical Society © 2011 RAS

Downloaded from http://mnras.oxfordjournals.org/ at FundaÃ§Ã£o CoordenaÃ§Ã£o de AperfeiÃ§oamento de Pessoal de NÃ-vel Superior on February 25, 2014

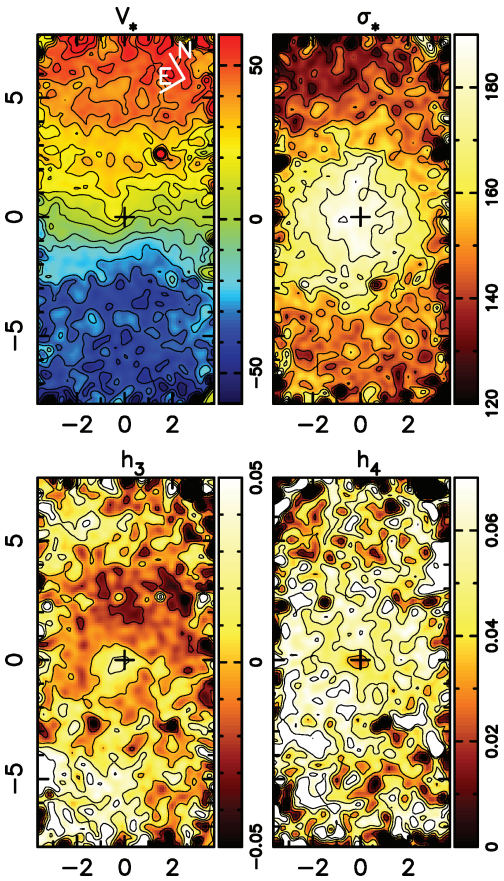

Figure 2. Top left: stellar centroid velocity field (km s^{-1}). Top right: stellar velocity dispersion (km s^{-1}). Bottom left: Gauss–Hermitte moment h_3. Bottom right: Gauss–Hermitte moment h_4.

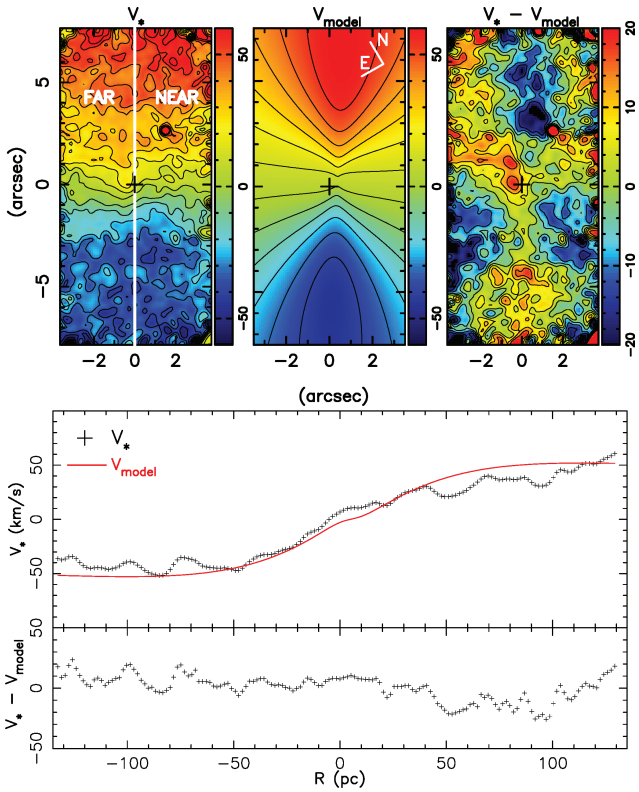

Figure 3. At the top, from left to right: stellar centroid velocity field (km s^{-1}), model velocity field (km s^{-1}), residuals between stellar and model velocity field (km s^{-1}). Note the change of scale between the velocity fields and the residuals. The straight white line indicates the position of the line of nodes. At the bottom we show the stellar and model velocity curve along the major axis (top) and the residuals along the major axis (bottom).

The stellar velocity dispersion (top-right panel of Fig. 2) decreases from decreases from ≥190 km s^{-1} at the nucleus to ≈140 km s^{-1} at a radial distance of ≈5 arcsec (≈85 pc from the nucleus), with an average value of 153 km s^{-1}. Calculated errors are ≈15 km s^{-1}.

The Gauss–Hermite moments h_3 and h_4 (bottom panels of Fig. 2) are measures of the skewness and the kurtosis, respectively, of the line-of-sight velocity distribution (LOSVD). Errors are of the order of 0.03 for both h_3 and h_4. There is a ring-like region of ≈0 values at ≈20 pc from the nucleus in the h_3 map indicating that the LOSVD in this region has a Gaussian profile. h_3 rises to ≈0.05 within a region with radius ≈17 pc centred on the nucleus and also beyond the ring, indicating a skewness of the LOSVD towards the red in these regions. Low values of h_4 occur mainly in the nucleus ($h_4 \approx 0$) and the highest along the minor axis ($h_4 \approx 0.06$), indicating an LOSVD slightly more 'pointy' than a Gaussian at the later locations.

We have modelled the centroid velocity field using circular orbits in a Plummer potential (Plummer 1911) as we have successfully done in previous works (Barbosa et al. 2006; Riffel et al. 2008). This model is just a kinematic model and does not take into account the full LOSVD of the stellar components. The stars are assumed to orbit in circular orbits in a thin disc coplanar with the main galactic disc, in spite of the fact that the stellar velocity dispersion is not negligible. In addition, we did not take into account the seeing and instrumental effects as our goal is only to derive the mean velocity field to be subtracted from the observed velocity field of the gaseous component.

The fit of the model gives a heliocentric systemic velocity of -125 ± 11 km s^{-1} taking into account measurement errors in the fit, a kinematic centre at horizontal and vertical coordinates of $X = 0.2$ arcsec and $Y = 0.4$ arcsec, respectively, relative to the peak flux in the continuum (adopted as the centre of the galaxy), and a position angle for the line of nodes of PA = 153° ± 1°. The displacement between the kinematic and photometric centre is smaller than the seeing radius, and it can thus be concluded that the two centres agree within the uncertainties. We have adopted a disc inclination of $i = 58°$, obtained from the apparent axial ratio (from NED[2]) under the assumption of a thin disc geometry, because the inclination is not well constrained in our multiparameter fitting procedure. The stellar centroid velocity field, the fitted circular model and the residuals between the stellar and modelled field are shown in the top panels of Fig. 3. The residuals are, at most locations, smaller than 10 km s^{-1}, for a total velocity amplitude of ≈100 km s^{-1}, revealing a good fit. Nevertheless, it can be noted that the isovelocity curves of the observed velocity field show a small 's-shape' distortion when compared to the model, associated with the bluest and reddest residuals. In the bottom of Fig. 3 we show the observed and model velocities extracted within a pseudo-slit ≈0.2 arcsec wide, oriented along the major axis at PA = 153°, in order to illustrate better the fit. The systemic velocity obtained from the fit $V_s = -125 \pm 11$ km s^{-1} was adopted as the galaxy systemic velocity and subtracted from the stellar and gaseous centroid velocities.

[2]NASA/IPAC Extragalactic Database.

Downloaded from http://mnras.oxfordjournals.org/ at FundaÃ§Ã£o CoordenaÃ§Ã£o de AperfeiÃ§oamento de Pessoal de NÃ-vel Superior on February 25, 2014

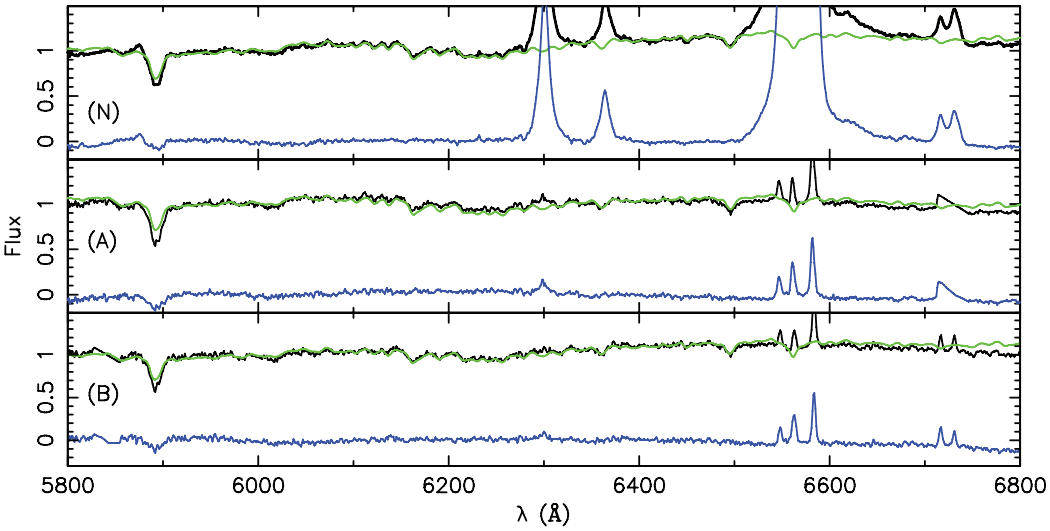

Figure 4. Observed spectrum (black), fitted absorption spectrum (green) and residual spectrum (blue) for three different regions.

4.2 Gaseous kinematics

In order to measure the gas kinematics we have subtracted the contribution from the stellar population. This was done using the STARLIGHT software (Cid Fernandes et al. 2005), in which the best-fitting absorption spectra is obtained through the technique of spectral synthesis. An illustration of the procedure is shown in Fig. 4 for the nucleus and for locations A and B (Fig. 1).

The gas kinematics – centroid velocities and velocity dispersions – as well as the emission-line fluxes were obtained by the fit of Gaussians to the [N II], Hα, [O I] and [S II] emission lines in the subtracted spectra. We note that the [S II] line could only be measured in the half of the field where the line profile was not affected by the gap between the CCDs.

Errors were estimated from Monte Carlo simulations in which Gaussian noise is added to the spectra. 100 iterations were performed. Errors in the velocity, flux distribution and velocity dispersion measurements for the [N II] and Hα emission lines have their lowest values within a radius of 2 arcsec and grow when approaching the borders of the field, where the signal-to-noise ratio is lower. The error values in both the velocity and velocity dispersion are, respectively, $\approx$10 km s^{-1} for the inner region and $\approx$20 km s^{-1} for the outer region. For the emission-line fluxes they are, respectively, $\approx$10 per cent for the inner region and $\approx$25 per cent for the outer region. In the case of the [S II] emission lines, errors in the velocity and velocity dispersion are $\approx$15 km s^{-1} and in the fluxes $\approx$20 per cent over the whole FOV. For the [O I] emission-line errors in the velocity and velocity dispersion are $\approx$10 km s^{-1} and $\approx$15 km s^{-1}, respectively, while in the fluxes they are $\approx$15 per cent. Regions with errors in velocity higher than $\approx$20 km s^{-1} were masked out.

Within the inner 1.5 arcsec it was also necessary to fit a broad component to Hα. The need for this became obvious when we examined line ratio maps such as [N II]/Hα: within a circular region with radius of $\approx$1 arcsec around the nucleus, the ratio decreased abruptly from values of $\approx$1.5 outside this region to values of $\approx$1 inside. By including a broad component within the inner region, the ratio between the narrow components [N II]/Hα showed a smooth transition between the two regions. In addition, by including the broad component in the fit, the width of the narrow component of Hα resulted practically the same as those of the [N II] emission lines, giving support to the presence of the broad component. As

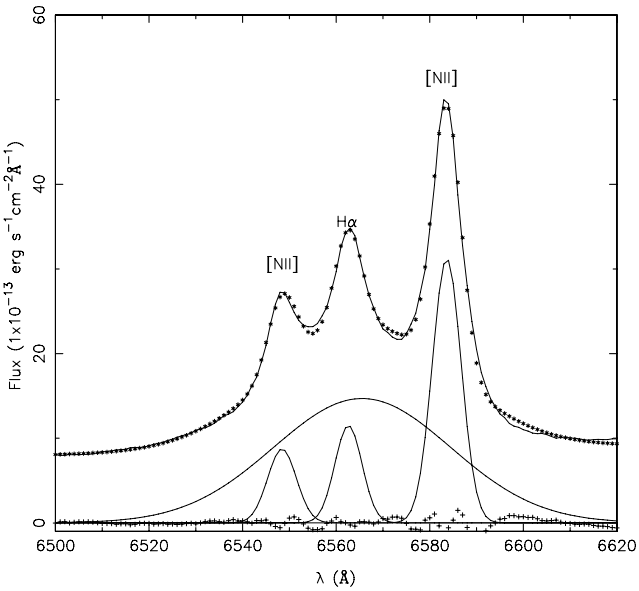

Figure 5. Upper panel: sample spectrum of the nucleus (black line) with the multi-Gaussian fit (represented by asterisks) to the emission lines superimposed. The individual Gaussian components are plotted below the spectrum along with the residuals between the spectrum of the nucleus and the fitted spectrum (crosses).

an additional 'sanity check' to the above procedure we also verified the resulting [N II]$\lambda\lambda$6583/6548 ratio which kept a value $\approx 3.0 \pm 0.2$ over the whole region where the fit to the broad line was performed.

An illustration of the fit of the [N II] $\lambda\lambda$6548,6583 Å lines and the broad and narrow Hα components is presented in Fig. 5 together with the residuals from the fit. Most of the flux of the broad component is well reproduced by a Gaussian with $\sigma = 862 \pm 37$ km s^{-1} and $V = -25 \pm 60$ km s^{-1}.

Centroid velocity maps for the emission lines are shown in Fig. 6 and velocity dispersion maps are shown in Fig. 7. The velocity fields in the [N II] and Hα are practically identical, and show that the gas is not in rotation along the same axis of the stars. If the gas were in rotation, the orientation would be perpendicular to that of the stellar rotation. Since the centroid velocities for the different emission

Downloaded from http://mnras.oxfordjournals.org/ at FundaÃ§Ã£o CoordenaÃ§Ã£o de AperfeiÃ§oamento de Pessoal de NÃ-vel Superior on February 25, 2014

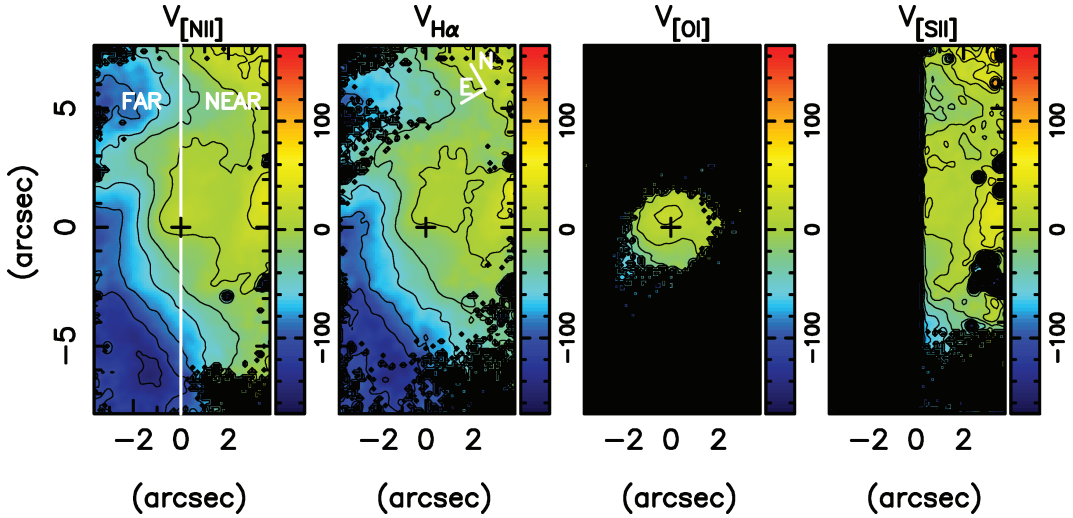

Figure 6. Gaseous centroid velocity (km s^{-1}) for the [N II], Hα, [O I] and [S II] emission lines.

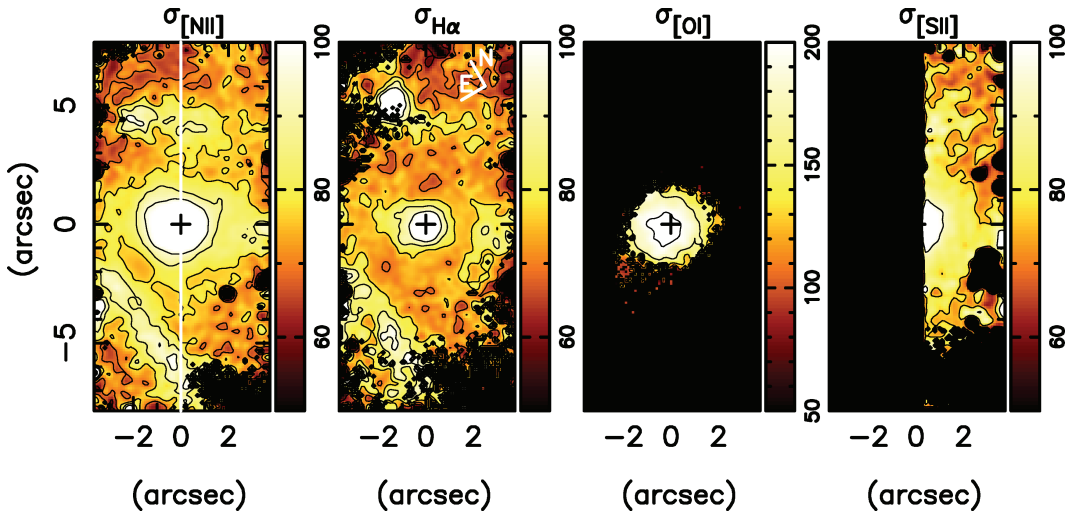

Figure 7. Velocity dispersion (km s^{-1}) for the [N II], Hα, [O I] and [S II] emission lines.

lines are almost identical, we chose the [N II] centroid velocity to represent the gaseous velocity field due to its higher signal-to-noise ratio over most of the field.

In order to isolate possible streaming motions we constructed a residual map by subtracting the stellar centroid velocity field from the gaseous one, under the assumption that the former represents the component of motion due to the galaxy gravitational potential. The residual map is shown in Fig. 8 along with the structure map and the [N II] velocity field previous to the subtraction of the stellar velocity field.

The Hα and [N II] velocity dispersion maps (hereafter $\sigma_{\mathrm{H}\alpha}$ and $\sigma_{[\mathrm{N\,II}]}$) are very similar. In most of the field both $\sigma_{[\mathrm{N\,II}]}$ and $\sigma_{\mathrm{H}\alpha}$ present the same values (within errors), usually ranging from 60 to 80 km s^{-1}. An exception occurs inside a radius of ≈0.8 arcsec from the nucleus, where $\sigma_{[\mathrm{N\,II}]}$ is about 20 km s^{-1} larger than $\sigma_{\mathrm{H}\alpha}$ (uncertainties being ≈5 km s^{-1} in this region). Also inside this radius $\sigma_{[\mathrm{N\,II}]}$ and $\sigma_{\mathrm{H}\alpha}$ reach their highest values, ≈140 km s^{-1} and ≈130 km s^{-1}, respectively. Away from the nucleus, an increase in the velocity dispersion is seen at two locations: ≈5 arcsec NW and ≈4 arcsec E from the nucleus, extending approximately diagonally in the IFU towards the S. These locations correspond to the largest blueshifts in the gas velocity fields.

5 LINE FLUXES AND EXCITATION OF THE EMITTING GAS

In Fig. 9, we present the integrated flux distributions for the [N II] λ6583 Å, the narrow component of Hα, [O I] λ6300 Å and [S II] λ6716 Å emission lines. While the [O I] flux distribution is compact, restricted to the inner ≈2 arcsec around the nucleus, the remaining flux distributions show an elongation from NW to SE, with the Hα flux distribution suggesting the presence of spiral arms at the top and bottom borders of the field. In the top left of the Hα panel, to the north of the nucleus, there is a small region with enhanced emission, suggesting the presence of an H II region at this location.

In Fig. 10, we show the line ratio maps [N II]/Hα and [O I]/Hα obtained using the narrow component of Hα, as well a gas density map, obtained from the [S II] λλ6717/6731 line ratio assuming an electronic temperature of 10 000 K (Osterbrock 1989). The

Downloaded from http://mnras.oxfordjournals.org/ at FundaÃ§Ã£o CoordenaÃ§Ã£o de AperfeiÃ§oamento de Pessoal de NÃ-vel Superior on February 25, 2014

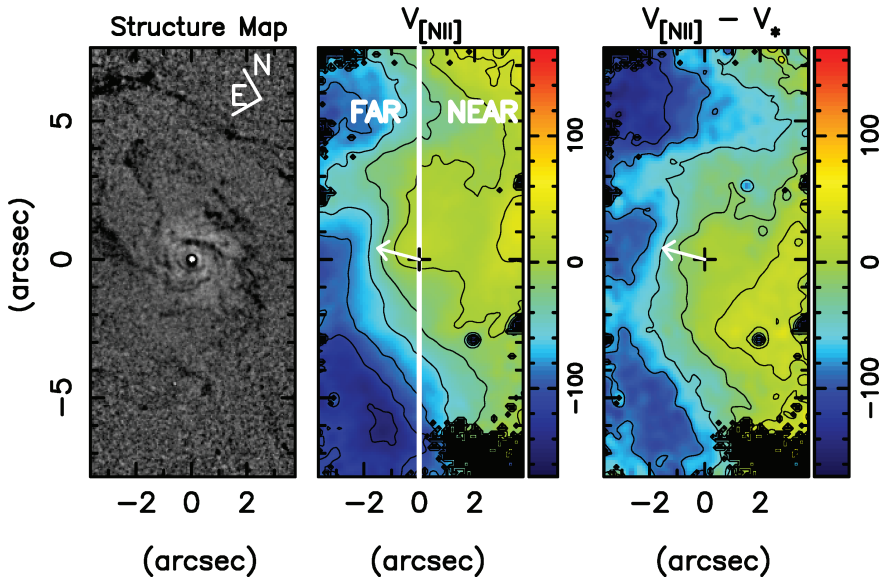

Figure 8. From left to right: structure map, gaseous centroid velocity (km s^{-1}) and the residual between gaseous centroid velocity and stellar velocity field (km s^{-1}). The vertical white line in the central panel indicates the position of the line of nodes, while the arrow in the right-hand panel shows the orientation of the compact radio jet.

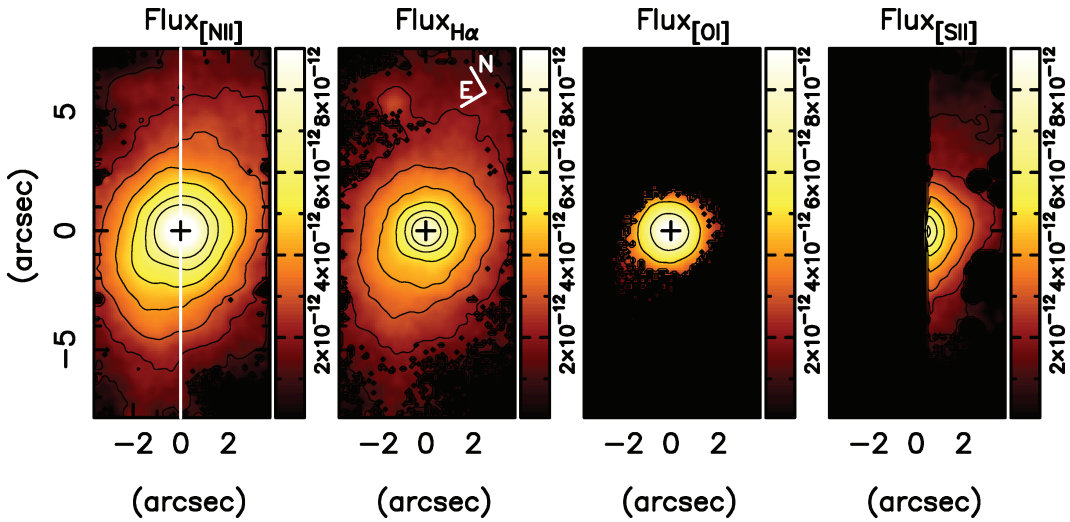

Figure 9. Maps of the [N II], Hα, [O I] and [S II] integrated fluxes (erg cm^2 s^{-1} per pixel).

[N II]/Hα ratio is 'LINER-like' – with [N II] stronger than Hα – over most of the IFU field. The only region with smaller ratios, typical of H II regions, is observed at the location of enhanced Hα emission to the north of the nucleus, supporting the interpretation that there is an H II region there. The highest values are observed at the nucleus (where the [N II]/Hα ratio is ≈3) and decrease outwards.

The [O I]/Hα ratio (central panel of Fig. 10) presents values typical of AGN, but there is a gradient in the values which range from ≈1.0 at ≈1 arcsec SW of the nucleus to ≈1.9 at ≈0.5 arcsec to the NE of the nucleus along PA ≈ 50°–60° (along the horizontal direction to the left in the figure). The asymmetry in the [O I]/Hα ratio in the nuclear region seems to be mostly due to an asymmetry in the [O I] flux distribution.

The [S II] density reaches its highest value within the inner arcsecond (17 pc), where it exceeds 10^3 cm^{-3}, decreasing to ≈500 cm^{-3} at 2 arcsec (34 pc) from the nucleus, the lowest measurable values are ≈300 cm^{-3} observed farther away.

6 DISCUSSION

6.1 Stellar kinematics

A previous study of the stellar kinematics along PA = 157° by Vega Beltrán et al. (2001), although on a much larger scale, has shown a smooth rotation pattern for the stars, which looks similar to ours, considering this specific PA. Nevertheless, our two-dimensional coverage allowed us to verify the presence of an s-shape distortion in the isovelocity contours. Elmegreen, Chromey & Johnson (1995) have argued for the presence of a nuclear bar extending up to ≈0.5 kpc (15 arcsec) from the nucleus along PA ≈ 140°, inferred from the fit of elliptical isophotes to a continuum *J*-band image of M81. This bar is thus oriented only 10° from the vertical direction in Fig. 3 and extends beyond the FOV of our observations with reaches only 7.5 arcsec along this PA. We may thus be sampling a region inside the bar and both the presence of an s-shape distortion in the isovelocity contours and the x-shaped residuals in Fig. 3 are

Downloaded from http://mnras.oxfordjournals.org/ at FundaÃ§Ã£o CoordenaÃ§Ã£o de AperfeiÃ§oamento de Pessoal de NÃ-vel Superior on February 25, 2014

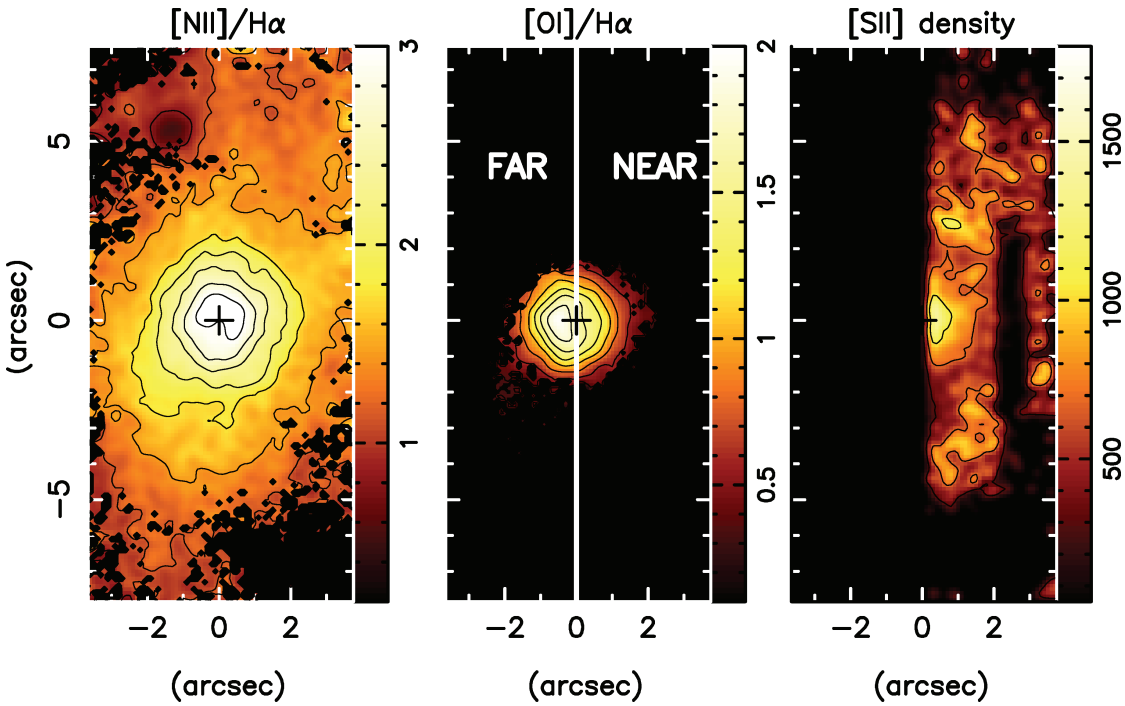

Figure 10. From left to right: [N II]/Hα and [O I]/Hα emission-line ratios and the gas density (cm^{-3}) derived from the [S II] line ratio.

consistent with the elongated pattern of stellar orbits required to support a bar.

Considering an inclination of 58°, the amplitude of the rotation curve to each side of the nucleus reaches at most 60 km s^{-1}. This is much smaller than the velocity dispersion observed over the whole IFU field, which ranges from 140 to 190 km s^{-1}. We thus can use the stellar velocity dispersion map (Fig. 3) alone to obtain a virial estimate for the mass of the bulge. The average value of the velocity dispersion inside a radius of 3.5 arcsec (the maximum covered by our observations along the shorter axis of the IFU) is 167 km s^{-1}. In order to obtain the velocity dispersion of the bulge this value needs to be corrected according to equation (2) of Jørgensen, Franx & Kjærgaard (1995). Adopting an effective radius of $r_e = 66.2$ arcsec (Baggett, Baggett & Anderson 1998) we obtain 162 km s^{-1}, which is in good agreement with previous measurements (Vega Beltrán et al. 2001; Nelson & Whittle 1995; Beifiori et al. 2009). This leads to a virial mass of 2.1×10^8 M$_\odot$.

The above bulge velocity dispersion can also be used to estimate the central black hole mass using the M–σ relation (Tremaine et al. 2002; Gültekin et al. 2009), which results in $M_{\rm BH} = 5.5^{+3.6}_{-2.0} \times 10^7$ M$_\odot$. This value is consistent with the previous virial estimate of the total mass, and is of the same order of the values obtained by Devereux et al. (2003) and Beifiori et al. (2009) for the mass of the black hole, which are 6.7×10^7 and 3.7×10^7 M$_\odot$, respectively, when rescaled to the distance we adopted in this study.

6.2 Gaseous kinematics and excitation

On kiloparsec scales, the H I gas kinematics (Rots 1975) shows a similar rotation pattern to that of our stellar velocity field, and our PA = 153° of the line of nodes is comparable to the value of PA = 150° obtained by Goad (1976). Nevertheless, on the scales probed by our observations, the gas kinematics is very different from that of the stars. This was already noted by Goad (1976), who obtained the kinematics for the [N II] λ6583 Å and Hα emission lines in the inner 1 kpc of the galaxy and found the gaseous velocity field to be complex and impossible to describe by simple rotation alone. A disturbed kinematics was also found by Vega Beltrán et al. (2001) in the [O III] λ5007 emission-line gas. But they argue that their long-slit data along PA = 157° suggest that there is a circumnuclear Keplerian disc of ionized gas. Our Hα kinematics along this axis does not show this behaviour, probably because [O III] and Hα are probing distinct kinematics.

The gas isovelocity curves in our Fig. 6 suggest a kinematic major axis almost perpendicular to that of the stars and even more than one rotation centre. Nevertheless, the location of these apparent rotation centres, as well as the isovelocity contours in their vicinity, correlates with the locations of increased velocity dispersions (Fig. 7) suggesting that these regions are related to shocks in the gas. The overall orientation of these features seems also to be the same as those of the dust lanes in the structure map. We also note that most blueshifts are in the far side of the galaxy, suggesting inflow towards the centre if most of the gas is in the galaxy plane. In this case the shocks mentioned above could be responsible for dissipating angular momentum and allowing the gas to flow in towards the nucleus to feed the AGN. If a nuclear bar is present, as suggested by the photometry of Elmegreen et al. (1995) and by the distortions of the stellar isovelocity curves, this bar could also play a role in channelling gas inwards from the outer regions of the galaxy. This possibility is supported by the gas flux maps (Fig. 9), which are elongated towards the bar orientation.

If the gas is not in the galaxy plane, the observed blueshifts could be due to outflow to high galactic latitudes. Relevant to this hypothesis is the observation of a compact one-sided radio jet by Bietenholz et al. (2000) and, more recently, by Markoff et al. (2008). This jet is seen at an average position angle of PA = 50° ± 6° and extends only to ≈ 0.003 arcsec from the nucleus (Markoff et al. 2008). We plotted its direction in Fig. 8. Although it points to some blueshifts observed beyond ≈1.5 arcsec to the left of the nucleus in the figure, the gas closer to the nucleus (thus at the scale of the jet

Downloaded from http://mnras.oxfordjournals.org/ at FundaÃ§Ã£o CoordenaÃ§Ã£o de AperfeiÃ§oamento de Pessoal de NÃ-vel Superior on February 25, 2014

extent) is not observed in blueshift, suggesting that the blueshifts are not related to the radio jet.

Within the inner arcsecond around the nucleus, the increase in the gas velocity dispersion may be related to the compact nuclear jet at PA = 50° in interaction with the surrounding gas. Coincidently, this is approximately the PA along which we observe an increase in the [O I]/Hα line ratio (Fig. 10), a well-known signature of shocks (Baldwin, Phillips & Terlevich 1981; Osterbrock 1989).

6.3 Estimating the mass accretion flow

The residual blueshifts observed in Fig. 8 reach high values of $\approx -100\,\mathrm{km\,s^{-1}}$ in three regions in the far side of the galaxy. If we assume that the gas is located in the galaxy plane, this means that the gas is inflowing to the nucleus and we can thus estimate the rate of mass inflow. In order to do this, we assume that the three regions channel gas towards the nucleus. Assuming a similar geometry for the three regions, the total gas mass inflow will be three times the flow in one region. The flux of matter crossing one region can be calculated as:

$$\phi = N_{\mathrm{e}} v \pi r^2 m_{\mathrm{p}} f,$$

where N_{e} is the electron density, v is the streaming velocity of the gas towards the nucleus, m_{p} is the mass of the proton, r is the cross-section radius of the inflow and f is the filling factor. For the purpose of the present calculation, we adopt a cross-section radius of 17 pc and a typical value for the filling factor of $f = 0.001$.

The velocity residuals in the three blueshifted regions on the far side of the galaxy, which we have interpreted as due to streaming motions, range from $\approx -80\,\mathrm{km\,s^{-1}}$ to $\approx -120\,\mathrm{km\,s^{-1}}$ (Fig. 8). As we have assumed that these streaming motions occur in the plane of the galaxy, we need to correct these values for the inclination of the galaxy $i = 58\overset{\circ}{.}4$. The resulting average velocity for the streaming motions is $v = -117\,\mathrm{km\,s^{-1}}$. For $N_{\mathrm{e}} = 500\,\mathrm{cm^{-3}}$ (obtained from the [S II] ratio) and $v = -117\,\mathrm{km\,s^{-1}}$, we obtain the value for the total inflow of ionized gas mass of $\phi \approx 4.0 \times 10^{-3}\,\mathrm{M_{\odot}\,yr^{-1}}$.

We note that the above calculation is only a rough estimate, as it depends on uncertain parameters, such as the geometry of the flow. We point out also the fact that the estimated inflow rate is in ionized gas and is thus a lower limit to the total inflow rate, as it may be only the ionized 'skin' of a more massive inflow in non-emitting neutral gas. The presence of molecular gas closer than $\approx$300 pc from the nucleus seems to be ruled out by the observations of Sakamoto et al. (2001), who found that molecular gas is mainly on a 'pseudo-ring' or spiral arm at about 500 pc from the nucleus.

We now compare the estimated inflow rate of ionized gas to the mass accretion rate necessary to produce the luminosity of the LINER nucleus of M81, calculated as follows:

$$\dot{m} = \frac{L_{\mathrm{bol}}}{c^2 \eta},$$

where η is the efficiency of conversion of the rest mass energy of the accreted material into radiation. For LINERs, it has been concluded that, in most cases, the accretion disc is geometrically thick, and optically thin (Nemmen et al. 2006; Yuan 2007). This type of accretion flow is known as Radiatively Inefficient Accretion Flow (RIAF) (Narayan 2005), and has a typical value for $\eta \approx 0.01$. The nuclear luminosity can be estimated from the X-ray luminosity of $L_{\mathrm{X}} = 3.2 \times 10^{40}\,\mathrm{erg\,s^{-1}}$ (Ho 1999), using the approximation that the bolometric luminosity is $L_{\mathrm{B}} \approx 10 L_{\mathrm{X}}$. We use these values to derive an accretion rate of $\dot{m} = 5.65 \times 10^{-4}\,\mathrm{M_{\odot}\,yr^{-1}}$.

Comparing this accretion rate $\dot{m}$ with the mass flow of ionized gas along the three regions derived above ϕ, we conclude that $\phi \approx 7\,\dot{m}$. Thus, the inflow of ionized gas in the inner tens of parsecs of M81 is already of the order of the one necessary to feed its AGN.

6.4 PCA tomography

In order to try to extract more information from the complex gas kinematics of the nuclear region, we have used an alternative approach which has been successfully applied to reveal small-scale features around nearby AGN by Steiner et al. (2009): the method of PCA. The method, which is applied directly to the calibrated data cube, allows the separation of the information, originally presented in a system of correlated coordinates, into a system of uncorrelated coordinates ordered by principal components of decreasing variance. These new coordinates called 'eigenspectra' (eigenvectors which are functions of wavelength) reveal spatial correlations and anticorrelations associated with features that may be associated with emission-line regions. The projection of the data on to these new coordinates produces images called 'tomograms', which represent slices of the data in the space of the eigenvectors. In order to apply this technique, we first corrected the data for differential atmospheric refraction and applied a Richardson–Lucy deconvolution algorithm (Richardson 1972; Lucy 1974) to the data cube using six iterations. A larger number of iterations did not improve the results, as also verified in previous works. A discussion about this point can be found in Morelli et al. (2010) and Michard (1996). The real point spread function (PSF) shows a small variation with wavelength, and a Gaussian with FWHM = 0.6 arcsec was found to be a good representation of the average PSF over the different wavelengths. We then applied the PCA to the inner $6 \times 14\,\mathrm{arcsec^2}$ and, in order to enhance the features in the vicinity of the active nucleus, also to the inner $4 \times 4\,\mathrm{arcsec^2}$ of the galaxy. We restricted the spectral range to $\lambda\lambda$ 6200–6700 Å, as there is no relevant information on the gas emission for $\lambda < 6200$ Å and the sulphur lines at $\lambda\lambda$ 6717,6731 are affected by falling in the gaps of the CCD, as previously explained.

The resultant eigenspectra and respective tomograms did not change significantly when the analysis was performed on either the inner $6 \times 14\,\mathrm{arcsec^2}$ or $4 \times 4\,\mathrm{arcsec^2}$ of the galaxy, the second eigenspectra and tomogram being an exception, as they presented small but significant changes. Because of the similarity we choose to primarily focus on the results corresponding to the larger spatial region for all eigenspectra and tomograms except for the second, for which both are shown.

We have performed a 'scree test' (see Steiner et al. 2009) to select the significant components – the ones not dominated by noise, which we concluded are the first eight (PC 1 to PC 8). The first six eigenspectra and corresponding tomograms are shown in Figs 11–13. PC 7 and PC 8, although significant, do not show any particular new structure.

Most of the variance is in the first eigenspectrum PC 1 (principal component 1, which contributes with 97.50 per cent of the variance), which is similar to the spectrum of the nucleus plus central stellar bulge (bottom-left panel of Fig. 11). The second tomogram, PC 2 (with 2.13 per cent of the variance), shows an anticorrelation between the nucleus and the stellar bulge. In the eigenspectrum 2 (bottom central panel of Fig. 11), one can clearly see a pure nuclear emission spectrum (positive values) anticorrelated with the stellar emission (negative values) – also evidenced by the 6500 Å stellar absorption feature, which appears in absorption in eigenspectrum 1 but appears inverted in the eigenspectrum 2. A somewhat conspicuous red Hα wing may be reminiscent of the double-peaked broad Hα reported by Bower et al. (1996). This feature is certainly weaker

© 2011 The Authors, MNRAS **413,** 149–161
Monthly Notices of the Royal Astronomical Society © 2011 RAS

Downloaded from http://mnras.oxfordjournals.org/ at FundaÃ§Ã£o CoordenaÃ§Ã£o de AperfeiÃ§oamento de Pessoal de NÃ-vel Superior on February 25, 2014

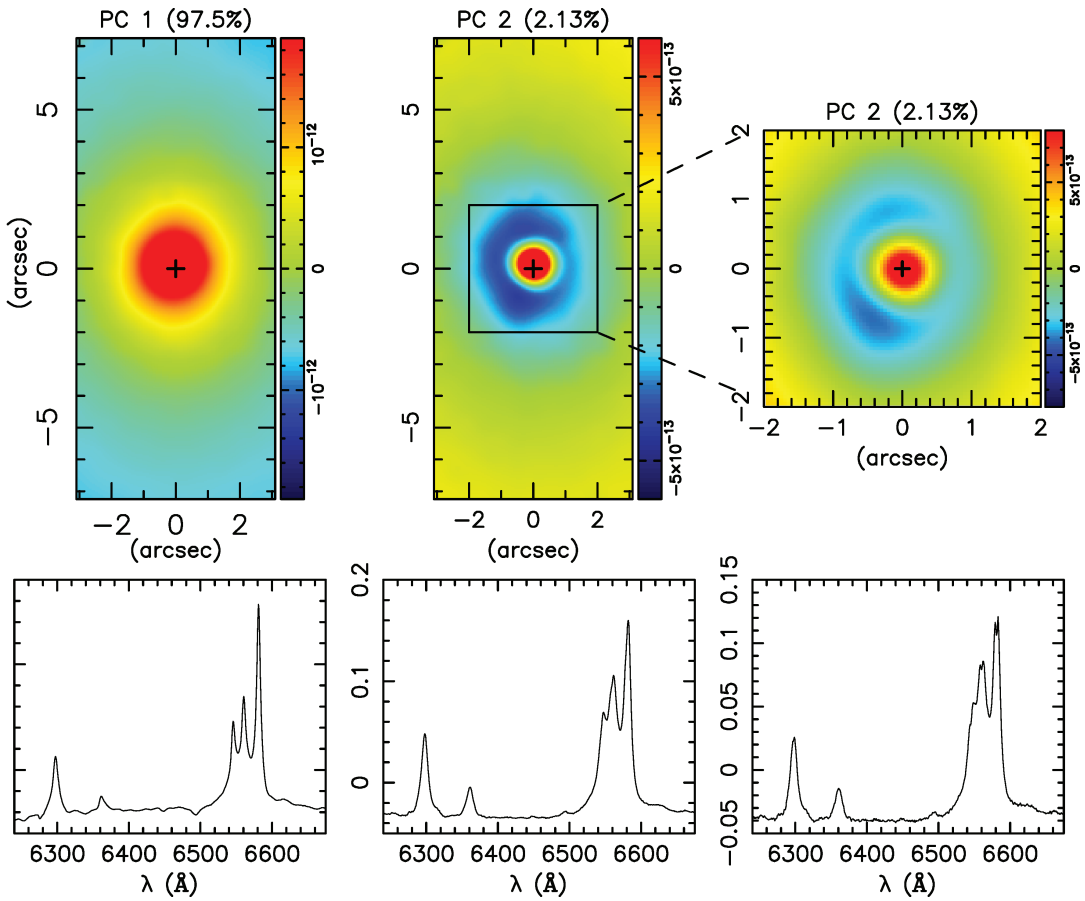

Figure 11. Left: first eigenspectra (bottom) and its respective tomograms (top); centre and right: second eigenspectra and tomogram resultant from the application of PCA to the larger (central panels) and smaller (right-hand panels) spatial regions. The square in the central panel shows the smaller central region where the PCA was also applied.

than reported by Bower et al. (1996) and the stellar feature at 6500 Å should not be confused with emission from the blue Hα wing. When the analysis is performed on the inner 4×4 arcsec^2 (right-hand panels of Fig. 11) a weak feature not seen in the centroid velocity maps appears: double peaks in the emission lines of Hα+[N II], with the blue and red peaks slightly blueshifted (≈ -80 km s^{-1}) and slightly redshifted (≈ 80 km s^{-1}), respectively, relative to the systemic velocity. The fact that the two peaks are correlated means that they are spatially coincident, that is, they come from the same region and are not spatially resolved. This can be interpreted as due to a compact bipolar outflow or rotation, not resolved in the data.

6.4.1 *Gas rotation versus outflow: feeding and feedback*

The third, fourth and fifth eigenspectra, PC 3 (with 0.25 per cent of the variance), PC 4 (0.07 per cent) and PC 5 (0.01 per cent), show peaks associated with the Hα+[N II] emission lines spatially anticorrelated with symmetric lobes (Fig. 12). The pattern in the tomogram of PC 5 is, in fact, very similar to that of PC 3, and we thus consider that PC 3+PC 5 correspond to one structure and PC 4, whose geometry in the tomogram is perpendicular to that of PC 3+PC 5, to another structure. These patterns can be explained either by a rotating gaseous disc or, else, by outflow of ionized gas, either a jet or a milder accretion disc outflow. A gaseous disc with such a behaviour was already proposed for NGC 4637 by Steiner et al. (2009). In the present case, however, we see two such structures with axes approximately orthogonal to each other. This can be explained by a simple model of a rotating disc and an outflow driven by this disc or by an unresolved accretion disc inside. This explains not only the existence of the two patterns, seen in PC 3+PC 5 and PC 4, but also the reason why they are orthogonal.

The immediate question that arises is which configuration, PC 3+PC 5 or PC 4, is associated with the rotating gaseous disc and which one is produced by the outflow. We propose that PC 3 and PC 5 are associated with the gaseous disc and PC 4 to the outflow. This interpretation is corroborated by the overall gas rotation seen in the galaxy as shown by the [N II] velocity field displayed in Fig. 8. The rotation axis seen in this figure (close to the nucleus) approximately coincides with the one seen in Fig. 12 for PC 3+PC 5 as does the sense of redshift–blueshift rotation. The PC 3 tomogram shows that the disc is within ≈ 50 pc from the nucleus and a comparison of this tomogram with the gas kinematics of Fig. 8 suggests that the disc is being fed by the gas circulating in the inner part of the galaxy. A compact disc in rotation around the nucleus has also been found in the H_2 kinematics of the inner few tens of parsecs of NGC 4151 (Storchi-Bergmann et al. 2010) and Mrk 1066 (Riffel & Storchi-Bergmann 2010).

Why do we see two eigenvectors, PC 3 and PC 5, with similar spectral structures? They are not really similar. In PC 3 the [O I] emission is seen in correlation with a bluish continuum while in PC 5 this emission is correlated with a reddish continuum. They very probably are associated with two regions affected by different

Downloaded from http://mnras.oxfordjournals.org/ at FundaÃ§Ã£o CoordenaÃ§Ã£o de AperfeiÃ§oamento de Pessoal de NÃ-vel Superior on February 25, 2014

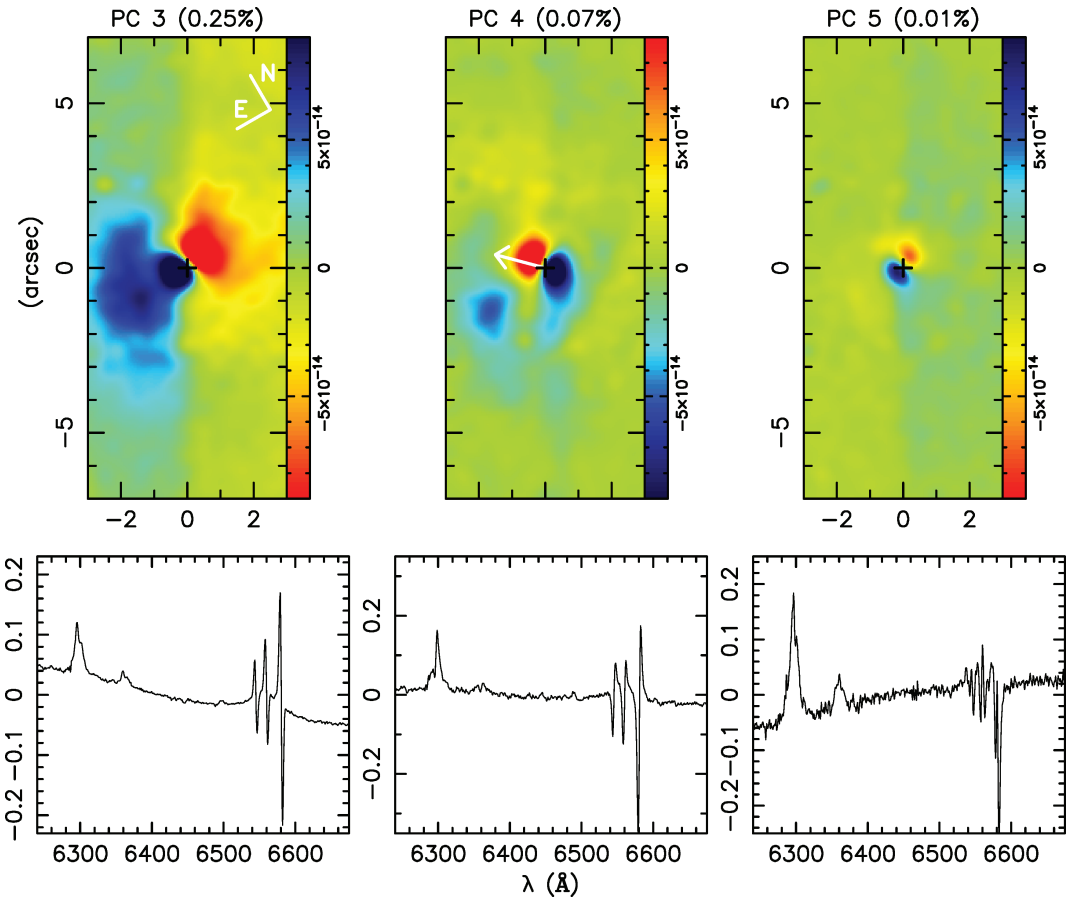

Figure 12. Bottom: third, fourth and fifth eigenspectra; top: corresponding tomograms. The correlations/anticorrelations in both eigenvectors and tomograms show gas movement and the approaching/receding sides can easily be identified.

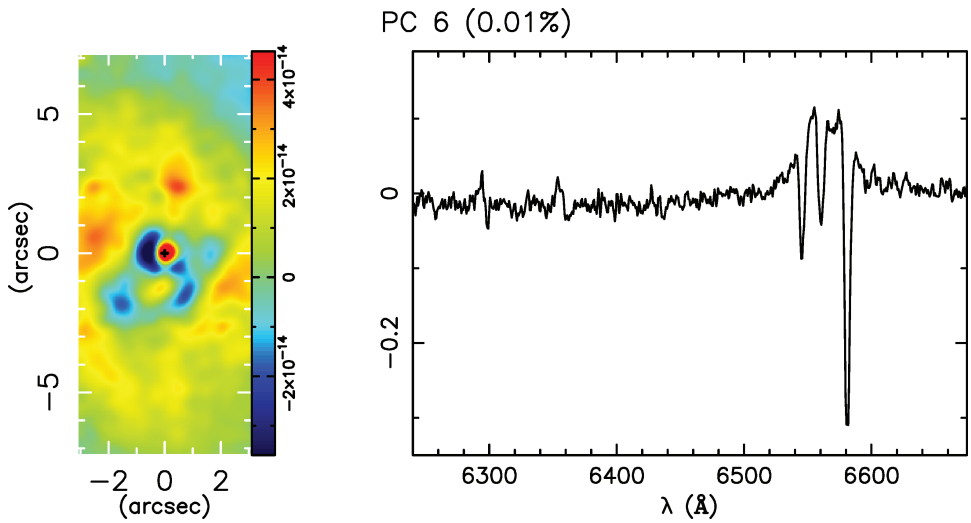

Figure 13. Left: tomogram of PC 6; right: eigenvector 6, showing the broad Hα component.

dust reddening or, else, by distinct scattering properties, or both. Thompson scattering by free electrons is wavelength independent but dust scattering or molecular Rayleigh scattering enhances blue characteristics. The partially ionized region responsible for the [O I] emission seen in tomogram 3 could be exposed to the central blue continuum source and scatter it to our line of sight, enhancing the blue aspect of the continuum emission.

We interpret PC 4 as due to an outflow, which most probably originates in the interaction of the radio jet discussed in Section 6.2 with the circumnuclear gas. We plotted the direction of the radio jet on tomogram 4 (arrow in Fig. 12). Considering that Markoff et al. (2008) argue that this jet precesses within 20° from this orientation, the jet direction approximately coincides with that of the axis of the presumed disc in tomogram 3. This is what one would expect

Downloaded from http://mnras.oxfordjournals.org/ at FundaÃ§Ã£o CoordenaÃ§Ã£o de AperfeiÃ§oamento de Pessoal de NÃ-vel Superior on February 25, 2014

if a conical outflow or jet is induced by an inner accretion disc; assuming that the axis of this inner accretion disc is aligned with the structure seen in tomogram 4, we have a self-consistent picture. As the highest energy photons are probably escaping perpendicular to the disc, we further predict that high-ionization species, not present in the spectral range of our observations, such as [O III], [Ne III] or He II, may be present in the blobs associated with PC 4.

Tomograms 3 and 4 also show that the [O I] emission is spatially correlated with the gas emission to the east-north of the nucleus. This is revealed in the eigenspectrum 3 by the fact that [O I] is correlated with the blueshifted emission (to the east), while in the eigenspectrum 4 it is correlated with the redshifted emission (to the north-east), in agreement with the previous result that the [O I] emission is enhanced towards the radio jet orientation of PA $\approx 50^\circ$. In addition, the [O I] profile has indications of double structure, being slightly redshifted. Although this question needs further studies we wonder whether this asymmetric [O I] enhancement is not related to the one-sided radio jet, perhaps due to shock heating of the partially ionized gas.

Finally, we show in Fig. 13 the tomogram (left-hand panel) and eigenspectrum (right-hand panel) of PC 6. The eigenspectrum shows that the unresolved broad component of Hα (see Fig. 5), which is confined to the red circle at the nucleus in the tomogram, is spatially anticorrelated with the narrow emission lines, which originate in the blue patches surrounding the nucleus.

7 CONCLUSIONS

We have measured the kinematics of the stars and ionized gas in the inner $120 \times 250\,\mathrm{pc}^2$ of M81 using integral field spectroscopy obtained with the GMOS instrument at the Gemini-North telescope with a spatial resolution of 10 pc at the galaxy. The main results of this paper are as follows.

(i) The stellar velocity field (centroid velocity) shows circular rotation with a major axis orientation of $\approx 153^\circ$, which is similar to that of the large-scale stellar rotation (as reported in previous works). But the two-dimensional coverage allowed the detection of deviations from pure rotation which can be attributed to stellar motions possibly associated with a nuclear bar (Elmegreen et al. 1995).

(ii) The stellar velocity dispersion of the bulge is $162 \pm 15\,\mathrm{km\,s^{-1}}$, in good agreement with previous measurements, resulting in an estimate of the black hole mass of $M_{\mathrm{BH}} = 5.5^{+3.6}_{-2.0} \times 10^7\,\mathrm{M}_\odot$.

(iii) The gaseous velocity field is completely distinct from the stellar one, and is dominated by blueshifts in the far side of the galaxy and a few redshifts in the near side. The subtraction of the stellar velocity field from the gaseous one confirms the presence of excess blueshifts of $\approx -100\,\mathrm{km\,s^{-1}}$ on the far side and some redshifts in the near side. If the gas is in the galaxy plane, these excesses can be interpreted as streaming motions towards the centre of the galaxy.

(iv) From the measured gas velocities and assumed geometry, we estimate an ionized gas mass flow rate of $\phi \approx 4.0 \times 10^{-3}\,\mathrm{M}_\odot\,\mathrm{yr}^{-1}$, a value about seven times the necessary accretion rate to power the AGN. However, this is only the mass flow rate in ionized gas. Most probably, the total inflow is much larger but is dominated by non-emitting gas.

(v) We have applied the technique of PCA to our data cube and find that the PCA reveals small-scale features not seen in the measured velocity field. The main features are: (1) an unresolved bipolar outflow or rotation at the nucleus; (2) a nuclear rotating disc within $\approx$50 pc from the nucleus; (3) a compact bipolar outflow approximately perpendicular to the disc.

(vi) The gas velocity field suggests that the nuclear disc is being fed by gas circulating in the galaxy plane.

(vii) An increase in the [O I]/Hα line ratio occurs at approximately the same orientation of a one-sided nuclear radio jet (PA $\approx 50^\circ$), which is also the approximate orientation of the bipolar outflow revealed by the PCA. The increase in the [O I]/Hα line ratio is thus probably due to the interaction of the jet with the circumnuclear gas, as this ratio is a well-known signature of shocks.

With our observations we are thus resolving both the feeding of the M81 AGN – via the compact disc and surrounding gas which seems to be replenishing the disc, and its feedback – via the compact outflow approximately perpendicular to the disc, probably driven by this disc or by an unresolved accretion disc inside.

ACKNOWLEDGMENTS

We acknowledge the referee for relevant suggestions which have improved the paper. This work is based on observations obtained at the Gemini Observatory, which is operated by the Association of Universities for Research in Astronomy, Inc., under a cooperative agreement with the NSF on behalf of the Gemini partnership: the National Science Foundation (United States), the Science and Technology Facilities Council (United Kingdom), the National Research Council (Canada), CONICYT (Chile), the Australian Research Council (Australia), Ministério da Ciência e Tecnologia (Brazil) and southeast CYT (Argentina). This work has been partially supported by the Brazilian institution CNPq.

REFERENCES

Adler D. S., Westpfahl D. J., 1996, AJ, 111, 735
Baggett W. E., Baggett S. M., Anderson K. S. J., 1998, AJ, 116, 1626
Baldwin J. A., Phillips M. M., Terlevich R., 1981, PASP, 93, 5
Barbosa F. K. B., Storchi-Bergmann T., Cid Fernandes R., Winge C., Schmitt H., 2006, MNRAS, 371, 170
Beifiori A., Sarzi M., Corsini E. M., Dalla Bontà E., Pizzella A., Coccato L., Bertola F., 2009, ApJ, 692, 856
Bietenholz M. F., Bartel N., Rupen M. P., 2000, ApJ, 532, 895
Bower G. A., Wilson A. S., Heckman T. M., Richstone D. O., 1996, AJ, 111, 1901
Bruzual G., Charlot S., 2003, MNRAS, 344, 1000
Cappellari M., Emsellem E., 2004, PASP, 116, 138
Cheng K. P., Collins N., Angione R., Talbert F., Hintzen P., Smith E. P., Stecher T., UIT Team, 1997, BAAS, 29, 1107
Cid Fernandes R., Mateus A., Sodré L., Stasińska G., Gomes J. M., 2005, MNRAS, 358, 363
Davies R. I., Maciejewski W., Hicks E. K. S., Tacconi L. J., Genzel R., Engel H., 2009, ApJ, 702, 114
Devereux N., Ford H., Jacoby G., 1997, ApJ, 481, L71
Devereux N., Ford H., Tsvetanov Z., Jacoby G., 2003, AJ, 125, 1226
Elmegreen D. M., Chromey F. R., Johnson C. O., 1995, AJ, 110, 2102
Emsellem E., Goudfrooij P., Ferruit P., 2003, MNRAS, 345, 1297
Emsellem E., Fathi K., Wozniak H., Ferruit P., Mundell C. G., Schinnerer E., 2006, MNRAS, 365, 367
Englmaier P., Shlosman I., 2004, ApJ, 617, L115
Erwin P., Sparke L. S., 1999, ASP Conf. Ser. Vol. 182. Galaxy Dynamics – A Rutgers Symposium. Astron. Soc. Pac., San Francisco, p. 243
Fathi K., Storchi-Bergmann T., Riffel R. A., Winge C., Axon D. J., Robinson A., Capetti A., Marconi A., 2006, ApJ, 641, L25
García-Burillo S., Combes F., Schinnerer E., Boone F., Hunt L. K., 2005, A&A, 441, 1011

Downloaded from http://mnras.oxfordjournals.org/ at FundaÃ§Ã£o CoordenaÃ§Ã£o de AperfeiÃ§oamento de Pessoal de NÃ-vel Superior on February 25, 2014

Goad J. W., 1976, ApJS, 32, 89
Gültekin K. et al., 2009, ApJ, 698, 198
Heckman T. M., 1980, A&A, 87, 152
Ho L. C., 1999, ApJ, 516, 672
Ho L. C., Filippenko A. V., Sargent W. L. W., 1996, ApJ, 462, 183
Iyomoto N., Makishima K., 2001, MNRAS, 321, 767
Jørgensen I., Franx M., Kjærgaard P., 1995, MNRAS, 276, 1341
Knapen J. H., 2005, Ap&SS, 295, 85
Laine S., van der Marel R. P., Rossa J., Hibbard J. E., Mihos J. C., Böker T., Zabludoff A. I., 2003, AJ, 126, 2717
Lucy L. B., 1974, AJ, 79, 745
Markoff S. et al., 2008, ApJ, 681, 905
Michard R., 1996, A&AS, 117, 583
Morelli L., Cesetti M., Corsini E. M., Pizzella A., Dalla Bontà E., Sarzi M., Bertola F., 2010, A&A, 518, A32
Mundell C. G., Shone D. L., 1999, MNRAS, 304, 475
Narayan R., 2005, Ap&SS, 300, 177
Nelson C. H., Whittle M., 1995, ApJS, 99, 67
Nemmen R. S., Storchi-Bergmann T., Yuan F., Eracleous M., Terashima Y., Wilson A. S., 2006, ApJ, 643, 652
Osterbrock D. E., 1989, Astrophysics of Gaseous Nebulae and Active Galactic Nuclei. University Science Books, Mill Valley, CA
Paturel G., Teerikorpi P., Theureau G., Fouqué P., Musella I., Terry J. N., 2002, A&A, 389, 19
Peimbert M., Torres-Peimbert S., 1981, ApJ, 245, 845
Plummer H. C., 1911, MNRAS, 71, 460
Pogge R. W., Martini P., 2002, ApJ, 569, 624
Richardson W. H., 1972, J. Opt. Soc. America, 62, 55
Riffel R. A., Storchi-Bergmann T., 2010, MNRAS, doi:10.1111/j.1365-2966.2010.17721.x
Riffel R. A., Storchi-Bergmann T., Winge C., McGregor P. J., Beck T., Schmitt H., 2008, MNRAS, 385, 1129
Rots A. H., 1975, A&A, 45, 43
Sakamoto K., Fukuda H., Wada K., Habe A., 2001, AJ, 122, 1319
Sánchez F. M., Davies R. I., Genzel R., Tacconi L. J., Eisenhauer F., Hicks E. K. S., Friedrich S., Sternberg A., 2009, ApJ, 691, 749
Shaw M. A., Combes F., Axon D. J., Wright G. S., 1993, A&A, 273, 31
Shlosman I., Begelman M. C., Frank J., 1990, Nat, 345, 679
Simões Lopes R. D., Storchi-Bergmann T., de Fátima Saraiva M., Martini P., 2007, ApJ, 655, 718
Steiner J. E., Menezes R. B., Ricci T. V., Oliveira A. S., 2009, MNRAS, 395, 64
Storchi-Bergmann T., Dors O. L., Jr, Riffel R. A., Fathi K., Axon D. J., Robinson A., Marconi A., Östlin G., 2007, ApJ, 670, 959
Storchi-Bergmann T., Lopes R. D. S., McGregor P. J., Riffel R. A., Beck T., Martini P., 2010, MNRAS, 402, 819
Tremaine S. et al., 2002, ApJ, 574, 740
Vega Beltrán J. C., Pizzella A., Corsini E. M., Funes J. G., Zeilinger W. W., Beckman J. E., Bertola F., 2001, A&A, 374, 394
Yuan F., 2007, inHo L. C., Wang J.-W., eds, ASP Conf. Ser. Vol. 373, The Central Engine of Active Galactic Nuclei. Advection-dominated Accretion: From Sgr A* to Other Low-luminosity AGNs. Astron. Soc. Pac., San Francisco, p. 95

This paper has been typeset from a TEX/LATEX file prepared by the author.

Downloaded from http://mnras.oxfordjournals.org/ at FundaÃ§Ã£o CoordenaÃ§Ã£o de AperfeiÃ§oamento de Pessoal de NÃ-vel Superior on February 25, 2014